




Article

A Compound Control Method Based on the Adaptive Linear Extended State Observer and Global Fast Terminal Sliding Mode Control for Inertially Stabilized Platform

Fa Fu , Xusheng Lei * and Rui Wang 

The School of Instrument Science and Opto-Electronics Engineering, Beihang University, Beijing 100191, China; zy2017501@buaa.edu.cn (F.F.); wangrui98@buaa.edu.cn (R.W.)

* Correspondence: xushenglei@buaa.edu.cn; Tel.: +86-136-2131-8676

Abstract: To realize high-performance control for the inertially stabilized platform, a compound control method based on the adaptive linear extended state observer and global fast terminal sliding mode control is proposed. For estimating the unknown disturbances of inertially stabilized platform, an adaptive linear extended state observer was developed. With the full use of the information of attitude and angular velocity, the adaptive bandwidth of an adaptive linear extended state observer can deal with the peaking phenomenon without introducing excessive noise. Furthermore, the adaptation law based on the global fast terminal sliding mode control for disturbance estimation compensation was developed, which can improve the disturbance estimation accuracy of the adaptive linear extended state observer, and the higher order terminal function in global fast terminal sliding mode control was replaced by the lumped disturbance estimation of adaptive linear extended state observer, which can improve the anti-interference ability of inertially stabilized platform, reduce the chattering problem, and improve the control performance. The asymptotic stability of the proposed control method has been proven by the Lyapunov stability theory. The effectiveness of the proposed method was validated by a series of simulations and experiments.

Keywords: inertially stabilized platform; adaptive linear extended state observer; global fast terminal sliding mode control; disturbances



Citation: Fu, F.; Lei, X.; Wang, R. A Compound Control Method Based on the Adaptive Linear Extended State Observer and Global Fast Terminal Sliding Mode Control for Inertially Stabilized Platform. *Machines* **2022**, *10*, 426. <https://doi.org/10.3390/machines10060426>

Academic Editors: Menghua Zhang and Ning Sun

Received: 27 April 2022

Accepted: 25 May 2022

Published: 26 May 2022

Publisher's Note: MDPI stays neutral with regard to jurisdictional claims in published maps and institutional affiliations.



Copyright: © 2022 by the authors. Licensee MDPI, Basel, Switzerland. This article is an open access article distributed under the terms and conditions of the Creative Commons Attribution (CC BY) license (<https://creativecommons.org/licenses/by/4.0/>).

1. Introduction

As the middle mechanism between the base and the carrier, the inertial stabilized platform (ISP) can isolate non-ideal interference effectively to realize a high-performance attitude control for the load line of sight (LOS) [1]. Therefore, it has become a common key piece of equipment in aerial remote sensing systems [2].

However, there exist multiple disturbances for the ISP system in the working process, including dynamic unbalanced torque, non-ideal angular motion and linear motion interference, coupling torque and friction interference torque, etc. [3,4]. These disturbances have non-Gaussian, slow time-varying, unknown frequency amplitude harmonics, norm-bounded and other complex structural characteristics [5]. The mechanism of the disturbances are so complex that it is hard for the ISP system to realize high-performance control in real applications [6].

To improve the system control accuracy and anti-disturbance ability in a complex environment, PID, robust control, sliding mode control (SMC), and neural network (NN) control methods have been proposed. PID control methods are often designed for the ISP system for simple structures [7]. However, the control performance is easily affected by complex environment disturbances. Robust control methods have shown high adaptability for parameter uncertainty in practical applications. Rezaei D. Mahdy [8] realized a high-performance control for the ISP system based on the robust control and predictive control method. However, the robust control method has corresponding conservative

characteristics with the improvement of the system's robustness. Although the control performance is easily worsened by the chattering phenomenon, the SMC method can deal with nonlinear systems with external disturbances and uncertainty effectively [9,10]. With the improvement requirement of the system robustness, the terminal sliding mode control (TSMC) scheme has been developed. A global fast terminal sliding mode control (GFTSMC) is proposed to guarantee the control system to converge to reference states robustly in desired time, which focused more in finite-time stabilization [11,12]. At present, GFTSMC has been applied in many fields, such as unmanned aerial vehicle (UAV) control, permanent magnet synchronous motor (PMSM) control, and so on [13,14]. After enough training, the NN control method can deal with nonlinear disturbances effectively [15,16]. However, it is hard to generate enough sampling data because of the complexity of the working environment. Combined with the SMC method, the adaptive NN control method is constructed without offline training [17]. However, the control performance is easily affected by the selection of the upper boundary of residual approximation errors.

Considering the system uncertainty, external disturbances and unmodeled dynamics as the lumped disturbance, the extended state observer (ESO) can estimate and eliminate disturbances effectively [18,19]. The parameter adjustment of linear ESO (LESO) is simple and convenient; therefore, LESO is widely used in practical engineering. With the LESO, the unstructural uncertainty of the DC motor can be dealt with effectively [20]. A. H. M. Sayem [21] proposed a LESO-based model repetitive control (MRC) method for the servo motor, which can compensate for periodic and non-periodic disturbances effectively. Considering the friction effect as external interference, the compound method based on the SMC and a reduced-order LESO is proposed for the friction compensation of omnidirectional mobile robots (OMRs) to realize high performance control [22]. However, the observation bandwidth of LESO has a great influence on its state estimation performance. The peaking phenomenon will be generated with the increment of bandwidth when the initial state of the system does not match the estimated state [23]. At the same time, the impact of input delay on the dynamic tracking error will become more and more obvious [24].

In this paper, in order to improve the ability to suppress various internal and external disturbances, and realize high control performance for the ISP system, a compound control method based on the adaptive linear ESO (ALESO) and the GFTSMC is proposed, which includes the following contributions:

- (1) Considering various internal and external disturbances as the lumped disturbance, the ALESO based on the adaptive bandwidth was developed to estimate the unknown lumped disturbance for the ISP system. With the full use of the information of attitude and angular velocity, it can deal with the peaking phenomenon without introducing excessive noise.

- (2) The adaptation law based on the GFTSMC for disturbance estimation compensation was developed to compensate for the disturbance estimation error of ALESO, which can improve the disturbance estimation accuracy of ALESO.

- (3) The GFTSMC is proposed to handle the ISP system nonlinearity, parameter variations, internal and external coupling, and disturbances. The higher order terminal function in GFTSMC is replaced by the lumped disturbance estimation of the ALESO, which can improve the anti-interference ability of ISP, reduce the chattering problem, and improve the control performance.

The outline of the paper is organized as follows: In Section 2, the nonlinear dynamic model of the ISP is constructed and disturbances are analyzed. In Section 3, the compound control method based on the ALESO and the GFTSMC is proposed to promote control performance, and the adaptation law is established. A series of simulations and experiments validate the effectiveness of the proposed control method in Section 4, followed by the conclusions in Section 5.

2. The Nonlinear Dynamic Model and Disturbances Analysis of ISP

A two-axis ISP is designed to locate faults of a high voltage line, whose length, width and height are 0.67 m, 0.17 m and 0.55 m. The ISP system is composed of the pitch and yaw gimbals, shown in Figure 1. The pitch and yaw gimbals are the inner gimbal and outer gimbal of the ISP system, respectively.

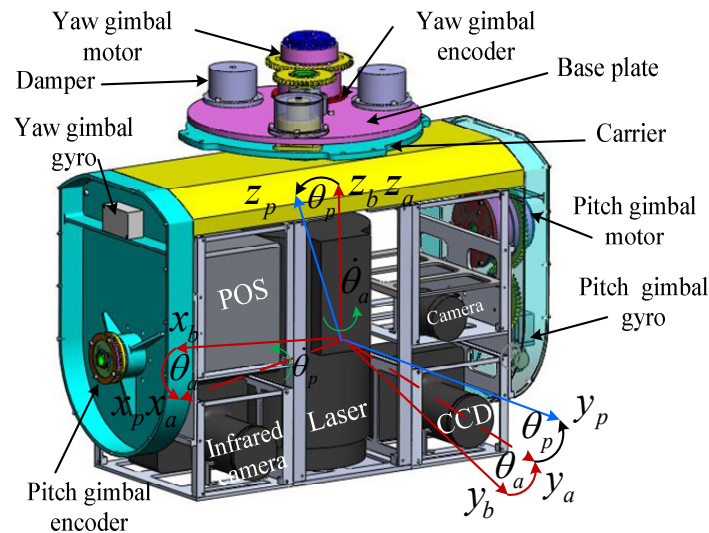


Figure 1. Two-gimbal ISP configuration diagram.

To get different faults information for high voltage lines, a long-focus camera and a short-focus camera, infrared camera, ultraviolet camera, and a 3D laser scanner were chosen as loads for the ISP system, which are located in the pitch box. The system is composed of duralumin LC4, with a total weight of 10.3 kg, and the total load weight of loads is 15.6 kg. To get enough torque to realize high-performance control, a large-torque EM-PIM375 motor with a reduction ratio of 1:4.5 was chosen. Moreover, to reject the high-frequency line vibration of vertical direction, four metal dampers with the same stiffness were installed uniformly between the base and the helicopter.

A high-performance position orientation system (POS) was chosen to provide the attitude angle information of the payloads, whose pitch angle and yaw angle measurement errors are less than 0.003° and 0.005° , respectively. Meanwhile, the open-loop optical fiber rate gyro, VG095M, was chosen to provide angular velocity information of the gimbals. Its constant drift is $15^\circ/\text{h}$. The rotary electric encoder DS-58-32-DF-C was introduced to the gimbals, whose precision is 0.003° . The ISP system was mounted on the bottom of the unmanned helicopter (UH). With the nonideal angle disturbances of UH, the LOS of the optical imaging sensors will deviate planed angles correspondingly. Since the POS is mounted on the same base of the different optical sensors, it can provide the angle information of the LOS of the optical sensors. Based on the measured information of POS, gyros, and encoders, the controller generates corresponding control signals to adjust the pitch and the yaw gimbal. Therefore, the LOS of the optical imaging sensors is adjusted correspondingly to eliminate angle errors to get precise images and video of the high-voltage wires and the electric towers.

As a typical multi-axis and multi-gimbal system, there exists a complex coordinate transformation process. The base plate coordinate axes x_b, y_b, z_b were fixed to the base plate, and the yaw coordinate axes x_a, y_a, z_a were fixed to the yaw gimbal. Furthermore, the pitch coordinate axes x_p, y_p, z_p were fixed to the pitch gimbal.

There is only the yaw angle θ_a about z_b between the base plate coordinate and the yaw coordinate. At the same time, only the pitch angle θ_p about x_a was used between the yaw coordinate and the pitch coordinate. The θ_a and θ_p can be measured by two encoders.

In order to explain the subsequent ISP model, define $B = p, a, b$ as the pitch, the yaw, and the base plate coordinate, respectively. $\omega_{tB}^B = [\omega_{tBx}^B \ \omega_{tBy}^B \ \omega_{tBz}^B]^T$ represents the angular velocity of the B coordinate axes with respect to the geographic coordinate axes expressed in the B coordinate axes. C_b^a and C_a^p represent the transformation matrixes from the base plate coordinate to the yaw coordinate and the yaw coordinate to the pitch coordinate, respectively. Based on the Newton–Euler theory, the dynamic model of the ISP system can be obtained as follows [25]:

$$\dot{\omega}_{tpx}^p = \frac{K_t K_e N^2 (\omega_{tax}^p - \omega_{tpx}^p) + N(N-1) R_m J_m \dot{\omega}_{tax}^p}{J_1 R_m} - \frac{(J_{pz} - J_{py}) \omega_{tpy}^p \omega_{tpz}^p}{J_1} + \frac{N K_t u_p}{J_1 R_m} + \frac{N T_{dm} + T_{dp}}{J_1} \quad (1)$$

$$\begin{aligned} \dot{\omega}_{tpz}^p = & \frac{J_{pz} \omega_{tpz}^p (\dot{\theta}_p + \omega_{tax}^a) \sin 2\theta_p}{2J_2} - \frac{J_2 \omega_{tax}^a \sin \theta_p \dot{\theta}_p}{J_2} \\ & - \frac{(J_{py} \omega_{tpy}^p \sin \theta_p)' \cos \theta_p + J_2 (\omega_{tay}^a \sin \theta_p)'}{J_2} \\ & + \frac{K_t K_e N^2 (\omega_{tbz}^a - \omega_{tax}^a) + N(N-1) R_m J_m \dot{\omega}_{tbz}^a}{J_2 R_m} \cos \theta_p \\ & - \frac{J_{py} \omega_{tpy}^p \omega_{tax}^a \cos^2 \theta_p}{J_2} + \frac{N K_t \cos \theta_p}{J_2 R_m} u_a \\ & + \frac{J_{px} \omega_{tpx}^p - (J_{ay} - J_{ax}) \omega_{tax}^a}{J_2} \omega_{tay}^a \cos \theta_p + \frac{N T_{dm} + T_{da}}{J_2} \cos \theta_p \end{aligned} \quad (2)$$

where the dots represent derivatives of a single variable, and the commas represent derivatives of the entire parenthesis. ω_{tax}^p , $\dot{\omega}_{tax}^p$, ω_{tbz}^a and $\dot{\omega}_{tbz}^a$ can be obtained by ω_{tb}^b , $\dot{\omega}_{tb}^b$ and the transformation matrices C_b^a and C_a^p . $J_p = \text{diag}(J_{px}, J_{py}, J_{pz})$ and $J_a = \text{diag}(J_{ax}, J_{ay}, J_{az})$ are the moment of inertia of pitch and yaw gimbal in three directions, respectively. $J_1 = J_{px} + N^2 J_m$, $J_2 = J_{az} + J_{pz} \cos^2 \theta_p + N^2 J_m$. J_m is the moment of inertia of the motor. K_t , K_e and R_m are the torque sensitivity, the back EMF constant, and the motor resistance, respectively. The N is the gear ratio of the motor. u_p and u_a are the voltage input applied on the pitch and yaw gimbal motor armature, respectively. T_{dp} and T_{da} are the torque disturbances imposed on the pitch and yaw gimbal, respectively, including mass imbalance torque and other unknown disturbances, such as wind disturbance. Moreover, T_{dm} is the torque disturbance imposed on the motor, which is caused by the residual vibration disturbances generated by the main rotor and the bearing friction, cogging, and imperfections in the motor.

With the analysis of the ISP system, the mass imbalance torque, the gimbal friction torque, the residual vibration disturbances generated by the main rotor, and the non-ideal angular motion interference generated by wind disturbance play important roles in the system errors.

The major part of T_{dL} ($L = p, a$) is the mass imbalance torque. In the ISP system exists a certain mass imbalance with the diversity of payloads. For real application, the maximum mass imbalance distance is required to be less than L_m , and the maximum weight of the payloads is often less than m_p , so the mass imbalance torque is $2m_p g L_m (\text{rand}(t) - 0.5)$. Meanwhile, in order to verify the effectiveness of the proposed control method, a certain random torque $A_w (\text{rand}(t) - 0.5)$ was used to simulate the wind disturbance. A_w is the amplitude of wind disturbance. Therefore, T_{dL} is represented by the disturbance with certain bounds in the ISP system

$$T_{dL} = (2m_p g L_m + A_w) \times (\text{rand}(t) - 0.5) \quad (3)$$

Friction torque is the first part of T_{dm} . The high-performance brushless DC torque motors are proposed to provide enough torque to adjust gimbal angle, where the sliding friction coefficient is μ . The weight and the radius of the motor gear are m_g and L_g , respectively. Since there exists a certain relationship between the friction torque and the

frequency of the motion of the ISP [17], the T_{dm1} is represented by the superposition of sinusoidal functions

$$T_{dm1} = \mu m_g g L_g (\sin(\omega_{dm} t) + \sin(2\omega_{dm} t)) \quad (4)$$

where ω_{dm} is the fundamental frequency of sinusoidal functions.

The second part of T_{dm} is the residual vibration disturbances. Since the high frequency periodic disturbances whose frequency surpass 10 Hz have been isolated effectively by the metal dampers, the certain sinusoidal torque $T_{dm2} = A_v \times (\sin(\omega_{dm} t) + \sin(2\omega_{dm} t))$ was used to simulate the residual periodic vibration disturbances. A_v is the amplitude of vibration disturbances. Therefore, T_{dm} is represented by the disturbance within certain bounds in the ISP system

$$T_{dm} = (\mu m_g g L_g + A_v) (\sin(\omega_{dm} t) + \sin(2\omega_{dm} t)) \quad (5)$$

In order to facilitate the design of the controller and for engineering practicality, (1) and (2) can be rewritten as

$$\dot{\omega}_{tpx}^p = f_1(t) + b_1 u_1 + g_1 d_1 \quad (6)$$

$$\dot{\omega}_{tpz}^p = f_2(t) + b_2 u_2 + g_2 d_2 \quad (7)$$

$$\text{where } f_1 = \frac{K_t K_e N^2 (\dot{\omega}_{tax}^p - \dot{\omega}_{tpx}^p) + N(N-1) R_m J_m \dot{\omega}_{tax}^p}{J_1 R_m} - \frac{(J_{pz} - J_{py}) \dot{\omega}_{tpy}^p \dot{\omega}_{tpz}^p}{J_1},$$

$$f_2 = \frac{J_{pz} \dot{\omega}_{tpz}^p (\dot{\theta}_p + \omega_{tax}^a) \sin 2\theta_p}{2J_2} - \frac{J_2 \omega_{tax}^a \sin \theta_p \dot{\theta}_p}{J_2} - \frac{(J_{py} \dot{\omega}_{tpy}^p \sin \theta_p)' \cos \theta_p + J_2 (\omega_{tax}^a \sin \theta_p)'}{J_2} \\ + \frac{K_t K_e N^2 (\dot{\omega}_{tbz}^a - \dot{\omega}_{tax}^a) + N(N-1) R_m J_m \dot{\omega}_{tbz}^a}{J_2 R_m} \cos \theta_p - \frac{J_{py} \dot{\omega}_{tpy}^p \omega_{tax}^a \cos^2 \theta_p}{J_2} \\ + \frac{J_{px} \dot{\omega}_{tpx}^p - (J_{ay} - J_{ax}) \omega_{tax}^a}{J_2} \omega_{tax}^a \cos \theta_p$$

$$b_1 = \frac{NK_t}{J_1 R_m}, b_2 = \frac{NK_t}{J_2 R_m} \cos \theta_p, u_1 = u_p, u_2 = u_a, g_1 = \frac{1}{J_1}, g_2 = \frac{\cos \theta_p}{J_2}, d_1 = NT_{dm} + T_{dp} + \Delta_1,$$

$d_2 = NT_{dm} + T_{da} + \Delta_2$, Δ_i includes the unmodeled friction, dead zone, hysteresis, and the unknown uncertainties of f_i , b_i , g_i and d_i , $i = 1, 2$.

3. The Compound Control Method of the ISP

Since $f_i, i = 1, 2$ are nonlinear and time-variant functions and contain the internal and external coupling of the gimbals, and there exist measurement errors and unknown disturbances, it is hard to generate suitable control commands to realize high-performance control. To improve the control performance, a compound control method based on the ALESO and the GFTSMC is proposed. The GFTSMC is proposed to handle the ISP system nonlinearity, parameter variations, internal and external coupling, and disturbances. In the conventional GFTSMC control law [14], the higher order terminal function $(\frac{L}{|s_{n-1}^{q/p}|} + \eta) s_{n-1}^{q/p}$ consists of the higher order sliding manifold s_{n-1} and four adjustable parameters: L , η , q and p . In order to improve the anti-interference ability of ISP, reduce the chattering problem, and enhance the control accuracy, the higher order terminal function is replaced by the lumped disturbance estimation of ALESO in the proposed control method.

Since the pitch and yaw gimbals have the same control structure, the pitch gimbal is chosen as an example. Let $\theta = \theta_p$, $\omega = \omega_{tpx}^p$, $b = b_1$, $u = u_1$, $f = f_1$, $gd = g_1 d_1$. The control flowchart is shown in Figure 2.

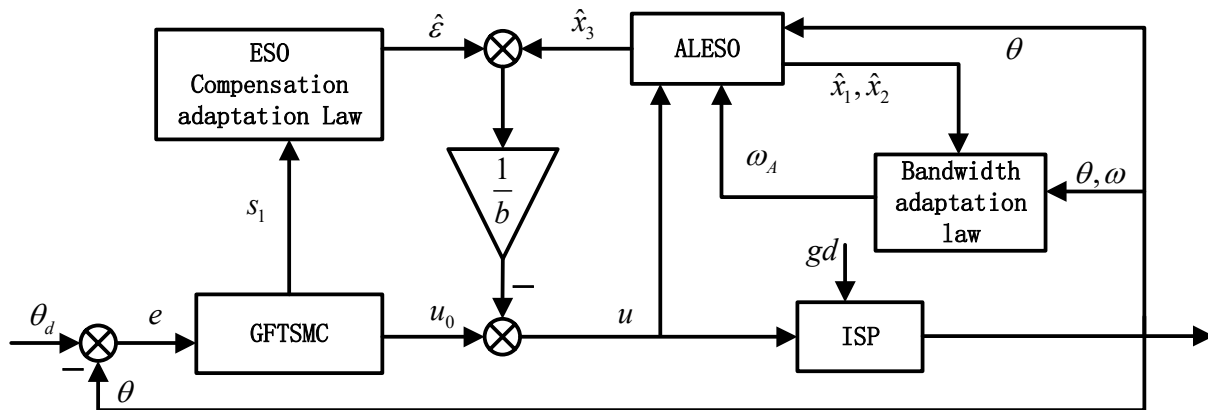


Figure 2. The flowchart of the compound method.

3.1. The ALESO

Define the lumped disturbance $D = gd$. For the dynamic model of ISP system, let $[x_1 \ x_2 \ x_3]^T = [\theta \ \omega \ D]^T$, where $x_i(t), i = 1, 2, 3$ are the state variables.

Assumption 1: The lumped disturbance D is bounded, satisfying $|D(t)| \leq H$, and $\dot{D}(t) = h(t)$ is bounded, satisfying $|h(t)| \leq \delta_{h(t)}$.

From the dynamic model (6), the expansion state model of ISP can be defined as follows:

$$\begin{cases} \dot{x}_1 = x_2 \\ \dot{x}_2 = f + bu + x_3 \\ \dot{x}_3 = h \end{cases} \quad (8)$$

For (8), in order to estimate the lumped disturbance D , we propose an ALESO

$$\begin{cases} e_1 = \hat{x}_1 - x_1 \\ \dot{\hat{x}}_1 = \hat{x}_2 - 3\omega_A(\tilde{\mathbf{x}})e_1 \\ \dot{\hat{x}}_2 = \hat{x}_3 + f + bu - 3\omega_A^2(\tilde{\mathbf{x}})e_1 \\ \dot{\hat{x}}_3 = -\omega_A^3(\tilde{\mathbf{x}})e_1 \end{cases} \quad (9)$$

where \hat{x}_1, \hat{x}_2 and \hat{x}_3 are the estimation value of x_1, x_2 and x_3 , e_1 is the error between \hat{x}_1 and x_1 . $\omega_A(\tilde{\mathbf{x}}) = \omega_0 \exp(-\tilde{\mathbf{x}}_o^T \delta \tilde{\mathbf{x}}_o)$, with $\tilde{\mathbf{x}}_o = [\tilde{x}_1 \ \tilde{x}_2]^T$, $\delta = \begin{bmatrix} 1/\delta & 0 \\ 0 & 1/(\omega_0^2 \delta) \end{bmatrix}$, is the bandwidth of ALESO, which is composed by the observation errors of x_1 and x_2 , and the constant $\delta > 0$ needs to be designed.

Remark 1: Compared with the LESO [26], ALESO contains system known state x_2 . The bandwidth of ALESO is an adaptive variable, not a fixed value, and the lumped disturbance estimation compensation ε will be designed later. The ALESO can deal with the peaking phenomenon without introducing excessive noise and improve the disturbance estimation accuracy. Moreover, the bandwidth change of the ALESO is driven by the observation errors $\tilde{\mathbf{x}}_o = [\tilde{x}_1 \ \tilde{x}_2]^T$, when $\tilde{\mathbf{x}}_o = [\tilde{x}_1 \ \tilde{x}_2]^T \rightarrow 0$, $\omega_A(\tilde{\mathbf{x}})$ will naturally reach to the maximum value ω_0 . And in order to avoid the estimation failure of ALESO due to large initial estimation error, define $\omega_A(\tilde{\mathbf{x}}) = \begin{cases} \omega_0 \exp(-\tilde{\mathbf{x}}_o^T \delta \tilde{\mathbf{x}}_o) & \omega_A(\tilde{\mathbf{x}}) \geq \omega_{min} \\ \omega_{min} & \omega_A(\tilde{\mathbf{x}}) < \omega_{min} \end{cases}$.

Convergence proof: Define. \square

$$\tilde{\mathbf{x}} = [\tilde{x}_1 \ \tilde{x}_2 \ \tilde{x}_3], \tilde{x}_i(t) = x_i(t) - \hat{x}_i(t), i = 1, 2, 3 \quad (10)$$

By subtracting (9) from (8), the error model of the ALESO can be obtained as follows:

$$\begin{aligned}\dot{\tilde{x}}_1(t) &= \tilde{x}_2(t) - 3\omega_A(\tilde{\mathbf{x}})\tilde{x}_1(t) \\ \dot{\tilde{x}}_2(t) &= \tilde{x}_3(t) - 3\omega_A(\tilde{\mathbf{x}})^2\tilde{x}_1(t) \\ \dot{\tilde{x}}_3(t) &= h(t) - \omega_A(\tilde{\mathbf{x}})^3\tilde{x}_1(t)\end{aligned}\quad (11)$$

Let $\zeta_i(t) = (\tilde{x}_i(t))/(\omega_0^{i-1})$, $i = 1, 2, 3$, according to (11), we can obtain

$$\dot{\zeta} = \omega_0 A_\zeta(\zeta)\zeta + B_\zeta \frac{h(t)}{\omega_0^2} \quad (12)$$

where $\zeta = [\zeta_1 \ \zeta_2 \ \zeta_3]^T \in \mathbb{R}^3$, $A_\zeta(\zeta) = \begin{bmatrix} -3\exp(-(\zeta_1^2 + \zeta_2^2)/\delta) & 1 & 0 \\ -3\exp(-(\zeta_1^2 + \zeta_2^2)/\delta) & 0 & 1 \\ -\exp(-(\zeta_1^2 + \zeta_2^2)/\delta) & 0 & 0 \end{bmatrix}$ and $B_\zeta = [0 \ 0 \ 1]^T$.

Theorem 1: For the ALESO (9), if $\delta > m^2/0.9$ ($m > 0$) and $V_\zeta(\zeta(0)) \leq m^2/(3\omega_0)$, there exist a constant $\sigma_i > 0$ and a finite time $T_1 > 0$, satisfying

$$|\tilde{x}_i(t)| \leq \sigma_i, \sigma_i = \frac{8\delta_{h(t)}}{\omega_0^{4-i}}, i = 1, 2, 3, \forall t \geq T_1 \quad (13)$$

Proof.: Considering the autonomous system of (12). \square

$$\dot{\zeta} = \omega_0 A_\zeta(\zeta)\zeta \quad (14)$$

For (14), define the Lyapunov function $V_\zeta(\zeta) = (1/\omega_0)\zeta^T P_0 \zeta$ with $A_0^T P_0 + P_0 A_0 = -I_3$, where $A_0 = \begin{bmatrix} -3 & 1 & 0 \\ -3 & 0 & 1 \\ -1 & 0 & 0 \end{bmatrix}$ and $P_0 = \begin{bmatrix} 1 & -0.5 & -1 \\ -0.5 & 1 & -0.5 \\ -1 & -0.5 & 4 \end{bmatrix}$. Then, the $\dot{V}_\zeta(\zeta)$ is

$$\dot{V}_\zeta(\zeta) = \zeta^T (A_\zeta(\zeta)^T P_0 + P_0 A_\zeta(\zeta)) \zeta \quad (15)$$

If $\delta > m^2/0.9$ and $V_\zeta(\zeta(0)) \leq m^2/(3\omega_0)$ is fulfilled, then $\|\zeta_0\|_2 \leq m$, $\zeta_0 = [\zeta_1 \ \zeta_2]$, $A_\zeta(\zeta)^T P_0 + P_0 A_\zeta(\zeta) < 0$, and $\zeta = 0$ of (14) is locally exponentially stable (Theorem 1 of [27]).

According to the exponential stability of (14) and Assumption 1, for (12), there exists an invariant set

$$B_0 \triangleq \left\{ \zeta \in \mathbb{R}^3: \|\zeta\|_2 \leq \frac{2\lambda_{\max}(P_0 B_\zeta)\delta_{h(t)}}{\omega_0^3} = \frac{8\delta_{h(t)}}{\omega_0^3} \right\} \quad (16)$$

For any $\zeta \notin B_0$ and $V_\zeta(\zeta) \leq m^2/(3\omega_0)$, one has

$$\dot{V}_\zeta(\zeta) = \zeta^T (A_\zeta(\zeta)^T P_0 + P_0 A_\zeta(\zeta)) \zeta + 2\zeta^T P_0 B_\zeta \frac{\delta_{h(t)}}{\omega_0^3} < 0 \quad (17)$$

Then, for all $t \geq T_1$, considering $\zeta_i(t) = (\tilde{x}_i(t))/(\omega_0^{i-1})$, $i = 1, 2, 3$ and (17), we can obtain

$$|\tilde{x}_i(t)| \leq \omega_0^{i-1} \|\zeta\|_2 \leq \frac{8\delta_{h(t)}}{\omega_0^{4-i}} = \sigma_i \quad (18)$$

3.2. The Compound Control Method Based on the ALESO and the GFTSMC

Assumption 2: In order to improve the lumped disturbance estimation accuracy of ALESO, define the lumped disturbance estimation compensation $\varepsilon = D - \hat{x}_3$, where the ε is an unknown bounded constant variable, and $\varepsilon \in \Omega_\varepsilon \triangleq \{\varepsilon \in \mathbb{R} : \varepsilon_{\min} \leq \varepsilon \leq \varepsilon_{\max}\}$. At the same time, define the $\hat{\varepsilon}$ as the estimation value of ε . The ε_{\min} , ε_{\max} are known values based on the system parameters.

Let the estimation error $\tilde{\varepsilon} = \hat{\varepsilon} - \varepsilon$. Combining Assumption 2, the adaptation law $\dot{\hat{\varepsilon}}$, with $\varepsilon_{\min} \leq \hat{\varepsilon}(0) \leq \varepsilon_{\max}$, can be defined as [28]

$$\dot{\hat{\varepsilon}} = \text{Proj}_{\hat{\varepsilon}}(\tau_{\hat{\varepsilon}}) = \begin{cases} 0, & \text{if } \hat{\varepsilon} \geq \varepsilon_{\max} \text{ and } \tau_{\hat{\varepsilon}} > 0 \\ 0, & \text{if } \hat{\varepsilon} \leq \varepsilon_{\min} \text{ and } \tau_{\hat{\varepsilon}} < 0 \\ \tau_{\hat{\varepsilon}} & \text{otherwise} \end{cases} \quad (19)$$

where $\tau_{\hat{\varepsilon}}$ is the adaptation function to be synthesized later, and the projection mapping used in (19) guarantees $\hat{\varepsilon} \in \Omega_{\hat{\varepsilon}} \triangleq \{\hat{\varepsilon} \in \mathbb{R} : \varepsilon_{\min} \leq \hat{\varepsilon} \leq \varepsilon_{\max}\}$.

Define the desired attitude angle θ_d and the angle tracking error as $e = \theta_d - \theta$. To achieve fast convergence and high precision, a global fast terminal sliding manifold is designed as:

$$\begin{cases} s_0 = e \\ s_1 = \dot{s}_0 + \alpha_0 s_0 + \beta_0 s_0^{q_0/p_0} \end{cases} \quad (20)$$

where $\alpha_0, \beta_0 > 0$, q_0 and p_0 ($p_0 > q_0$) are both positive odd integers.

From (20), when $s_1 = 0$, one has

$$\dot{s}_0 = -\alpha_0 s_0 - \beta_0 s_0^{q_0/p_0} \quad (21)$$

Remark 2: When s_0 is far away from zero, the approximate dynamics tends to $\dot{s}_0 = -\beta_0 s_0^{q_0/p_0}$, which is a fast terminal attractor. When s_0 approaches equilibrium $s_0 = 0$, the approximate dynamics now tends to $\dot{s}_0 = -\alpha_0 s_0$, which is a linear sliding mode, and s_0 decays exponentially. Because of the combination of fast terminal attractor and linear sliding mode, it can ensure the limited time of convergence and maintain the fastness of linear sliding mode as it approaches the equilibrium point.

The derivative of s_1 with respect to time is given by

$$\begin{aligned} \dot{s}_1 &= \ddot{s}_0 + \alpha_0 \dot{s}_0 + \frac{\beta_0 q_0}{p_0} s_0^{q_0/p_0-1} \\ &= \alpha_0 \dot{s}_0 + \frac{\beta_0 q_0}{p_0} s_0^{q_0/p_0-1} + (\ddot{\theta}_d - \ddot{\theta}) \\ &= \alpha_0 \dot{s}_0 + \frac{\beta_0 q_0}{p_0} s_0^{q_0/p_0-1} + (\ddot{\theta}_d - bu - f - D) \end{aligned} \quad (22)$$

Then, the control law u , the adaptation function $\tau_{\hat{\varepsilon}}$ can be designed as

$$\begin{aligned} u &= u_0 - \frac{1}{b}(\hat{x}_3 + \hat{\varepsilon}) \\ &= \frac{1}{b}(\alpha_0 \dot{s}_0 + \frac{\beta_0 q_0}{p_0} s_0^{q_0/p_0-1} + \ddot{\theta}_d - f + k_s s_1) - \frac{1}{b}(\hat{x}_3 + \hat{\varepsilon}) \end{aligned} \quad (23)$$

$$\tau_{\hat{\varepsilon}} = -\gamma_\varepsilon s_1 \quad (24)$$

where $k_s \in \mathbb{R}$ is a positive constant, $\gamma_\varepsilon \in \mathbb{R}$ is the learning rate.

Stability analysis: Define the Lyapunov function $V = \frac{1}{2}s_1^2 + \frac{1}{2\gamma_\varepsilon}\tilde{\varepsilon}^2$, then the \dot{V} is

$$\begin{aligned} \dot{V} &= s_1 \dot{s}_1 + \frac{1}{\gamma_\varepsilon} \tilde{\varepsilon} \dot{\tilde{\varepsilon}} \\ &= s_1 \left(\alpha_0 \dot{s}_0 + \frac{\beta_0 q_0}{p_0} s_0^{q_0/p_0-1} + (\ddot{\theta}_d - bu - f - D) \right) + \frac{1}{\gamma_\varepsilon} \tilde{\varepsilon} \dot{\tilde{\varepsilon}} \end{aligned} \quad (25)$$

Taking (23)–(24) into (25)

$$\begin{aligned}
 \dot{V} &= s_1 \left(\begin{aligned} &\alpha_0 \dot{s}_0 + \frac{\beta_0 q_0}{p_0} s_0^{q_0/p_0-1} + \ddot{\theta}_d - f - D \\ &-(\alpha_0 \dot{s}_0 + \frac{\beta_0 q_0}{p_0} s_0^{q_0/p_0-1} + \ddot{\theta}_d - f + k_s s_1) + (\hat{x}_3 + \hat{\varepsilon}) \end{aligned} \right) + \frac{1}{\gamma_\varepsilon} \tilde{\varepsilon} \dot{\hat{\varepsilon}} \\
 &= s_1 (-k_s s_1 + (\hat{x}_3 + \hat{\varepsilon}) - D) + \frac{1}{\gamma_\varepsilon} \tilde{\varepsilon} \dot{\hat{\varepsilon}} \\
 &= -k_s s_1^2 + s_1 \tilde{\varepsilon} + \frac{1}{\gamma_\varepsilon} \tilde{\varepsilon} \dot{\hat{\varepsilon}} = -k_s s_1^2 + \tilde{\varepsilon} (s_1 + \frac{1}{\gamma_\varepsilon} \dot{\hat{\varepsilon}}) \\
 &= -k_s s_1^2 \leq 0
 \end{aligned} \tag{26}$$

Then, with the control law u designed by (23), the sliding manifold $s_1 = 0$ is reachable.

Remark 3: It can be seen that the control law u given by (23) does not contain the higher order terminal function $(\frac{L}{|s_{n-1}|^{q/p}} + \eta)s_{n-1}^{q/p}$ in the conventional GFTSMC control law, which can improve the anti-interference ability of ISP, reduce the chattering problem, and improve the control performance. Moreover, the estimation compensation $\hat{\varepsilon}$ in u will help to enhance the estimation accuracy of ALESO for disturbances.

Remark 4: It should be noted that the projection mapping adaptation law (19) can guarantee $\tilde{\varepsilon}(s_1 + \frac{1}{\gamma_\varepsilon} \dot{\hat{\varepsilon}}) \leq 0$, thus guaranteeing $\dot{V} \leq 0$. Since $V \geq 0$, $\dot{V} \leq 0$, when $t \rightarrow \infty$, V is bounded, and it can be shown that $\hat{\varepsilon}$ is bounded.

Convergence time analysis: Ensuring that the system tracks the desired trajectory in finite time is the most significant feature of GFTSMC. The time that the system state converges to equilibrium can be adjusted by choosing the specific parameters.

From (20), when $s_1 = 0$, one has

$$s_1 = \dot{s}_0 + \alpha_0 s_0 + \beta_0 s_0^{q_0/p_0} = 0 \tag{27}$$

Which can be rewritten as

$$s_0^{-q_0/p_0} \frac{ds_0}{dt} + \alpha_0 s_0^{1-q_0/p_0} = -\beta_0 \tag{28}$$

Let $y_{s_0} = s_0^{1-q_0/p_0}$, then $\frac{dy_{s_0}}{dt} = \frac{p_0-q_0}{p_0} s_0^{-q_0/p_0} \frac{ds_0}{dt}$, and (28) can be written as

$$\frac{dy_{s_0}}{dt} + \frac{p_0-q_0}{p_0} \alpha_0 y_{s_0} = -\frac{p_0-q_0}{p_0} \beta_0 \tag{29}$$

So, the general solution of (29) is

$$\begin{aligned}
 y_{s_0} &= e^{-\int_0^t \frac{p_0-q_0}{p_0} \alpha_0 dt} \left(\int_0^t -\frac{p_0-q_0}{p_0} \beta_0 e^{\int_0^t \frac{p_0-q_0}{p_0} \alpha_0 dt} dt + C \right) \\
 &= e^{-\int_0^t \frac{p_0-q_0}{p_0} \alpha_0 dt} \left(\int_0^t -\frac{p_0-q_0}{p_0} \beta_0 e^{\frac{p_0-q_0}{p_0} \alpha_0 t} dt + C \right)
 \end{aligned} \tag{30}$$

When $t = 0$, $C = y_{s_0}(0)$, (30) then becomes

$$\begin{aligned}
 y_{s_0} &= e^{-\frac{p_0-q_0}{p_0} \alpha_0 t} \left(-\frac{p_0-q_0}{p_0} \beta_0 \frac{p_0}{(p_0-q_0)\alpha_0} e^{\frac{p_0-q_0}{p_0} \alpha_0 t} \Big|_0^t + y_{s_0}(0) \right) \\
 &= -\frac{\beta_0}{\alpha_0} + \frac{\beta_0}{\alpha_0} e^{-\frac{p_0-q_0}{p_0} \alpha_0 t} + y_{s_0}(0) e^{-\frac{p_0-q_0}{p_0} \alpha_0 t}
 \end{aligned} \tag{31}$$

And when $s_0 = e = 0$, which means that the angle tracking error is 0, $y_{s_0} = 0$, $t = t_s$, (31) then becomes

$$\begin{aligned}\frac{\beta_0}{\alpha_0} &= \frac{\beta_0}{\alpha_0} e^{-\frac{p_0-q_0}{p_0} \alpha_0 t_s} + y_{s_0}(0) e^{-\frac{p_0-q_0}{p_0} \alpha_0 t_s} \\ \frac{\beta_0}{\alpha_0} &= \left(\frac{\beta_0}{\alpha_0} + y_{s_0}(0) \right) e^{-\frac{p_0-q_0}{p_0} \alpha_0 t_s} \\ \frac{\beta_0 + \alpha_0 y_{s_0}(0)}{\beta_0} &= e^{\frac{p_0-q_0}{p_0} \alpha_0 t_s}\end{aligned}\quad (32)$$

where $y_{s_0}(0) = s_0(0)^{(p_0-q_0)/p_0} = e(0)^{(p_0-q_0)/p_0}$.

And we can conclude that the time from any initial state $s_0(0) = e(0) \neq 0$ converge to the desired state $s_0 = e = 0$ is

$$t_s = \frac{p_0}{\alpha_0(p_0 - q_0)} \ln \left(\frac{\alpha_0 e(0)^{(p_0-q_0)/p_0} + \beta_0}{\beta_0} \right) \quad (33)$$

By setting parameters α_0 , β_0 , q_0 and p_0 , the system can reach equilibrium in limited time t_s .

4. Simulations, Experiments and Discussion

4.1. Simulations

The corresponding parameters of ISP are shown in Table 1. The battery voltage of the DC motor of the ISP is 24 V. According to the technical documentation of the DC motor, the conversion relationship between the controller output and the real control voltage is $u_{\text{voltage}} = \frac{24 \text{ V}}{1000} u_{\text{controller}}$. Furthermore, \mathbf{J}_p and \mathbf{J}_a are $\text{diag}(0.20, 0.267, 0.46) \text{ kgm}^2$ and $\text{diag}(0.54, 0.475, 0.162) \text{ kgm}^2$, respectively. They were estimated numerically by SOLIDWORKS, and the corresponding disturbances, with $m_p = 30 \text{ kg}$, $g = 9.8 \text{ m/s}^2$, $L_m = 5 \text{ mm}$, $A_w = 1.5$, $\mu = 0.1$, $m_g = 0.5 \text{ kg}$, $L_g = 0.1 \text{ m}$, $A_v = 0.9$, $\omega_{dm} = 4.17$. $T_{dL} = (2.94 + 1.5) \times (\text{rand}(t) - 0.5)$ and $T_{dm} = (0.049 + 0.9) \times (\sin(4.71 t) + \sin(9.42 t))$ were added in simulations to verify the effectiveness of the compound control method.

Table 1. Parameters of the ISP system.

Parameter	Value	Unit
K_t	0.143	Nm/Amp
K_e	0.143	V/rad/s
R_m	7.56	Ohms
J_m	2.7×10^{-4}	kg m ²
N	50	

Moreover, to simulate the measurement noise, we added Gaussian noise with mean 0 and standard deviation 0.01 to the output of the dynamic model

$$d_{\text{noise}} = \text{normrnd}(0, 0.01) \quad (34)$$

The simulation environment is MATLABR2017b, where the simulation frequency and simulation step are 200 Hz and 0.005, respectively. All differential formulas are discretized by the Euler discretization method, and the simulation time is 10 s. Take the pitch gimbal as an example: the desired attitude angle $\theta_d = 5^\circ$, and the initial attitude angle $x_1(0) = -5^\circ$. The initial attitude angle velocity $x_2(0) = -0.15^\circ/\text{s}$. In addition, the value of $[\hat{x}_1(0) \ \hat{x}_2(0) \ \hat{x}_3(0)]^T = [0 \ 0 \ 0]^T$. Three different controllers, i.e., the proposed method, the linear SMC and the conventional GFTSMC, are tested in this part. They are given as

(1) The proposed method: the control law (23) with $\alpha_0 = 30$, $\beta_0 = 0.5$, $k_s = 25$, $q_0 = 5$, $p_0 = 9$, $\omega_0 = 30$, $\delta = 0.05$, $\omega_{\min} = 10$, $\hat{e}(0) = 0$, $[\varepsilon_{\min} \ \varepsilon_{\max}] = [-500 \ 500]$, $\gamma_\varepsilon = 1500$, and we test the disturbance estimation performance of LESO with the fixed bandwidth $\omega_o = 70$.

(2) SMC: the linear sliding manifold is $s = \dot{e} + ce$, and the control law is $u_{SMC} = \frac{1}{b} \left(c\dot{e} + \ddot{\theta}_d - f + k_s s + \eta \text{sgn}(s) \right)$ with $c = 30, k_s = 25, \eta = 120$.

(3) GFTSMC: the control law is $u_{GFTSMC} = \frac{1}{b} \left(\alpha_0 \dot{s}_0 + \frac{\beta_0 q_0}{p_0} s_0^{q_0/p_0-1} + \ddot{\theta}_d - f + k_s s_1 + \gamma s_1^{q_1/p_1} \right)$ with $\alpha_0 = 30, \beta_0 = 0.5, k_s = 25, q_0 = 5, p_0 = 9, q_1 = 13, p_1 = 15, \gamma = \frac{L}{|s_1^{q_1/p_1}|} + \eta, L = 100, \eta = 10$.

To validate the effectiveness of the proposed method, control performances, control voltages, disturbance estimations, disturbance estimation errors and observer bandwidth are shown in Figures 3–7.

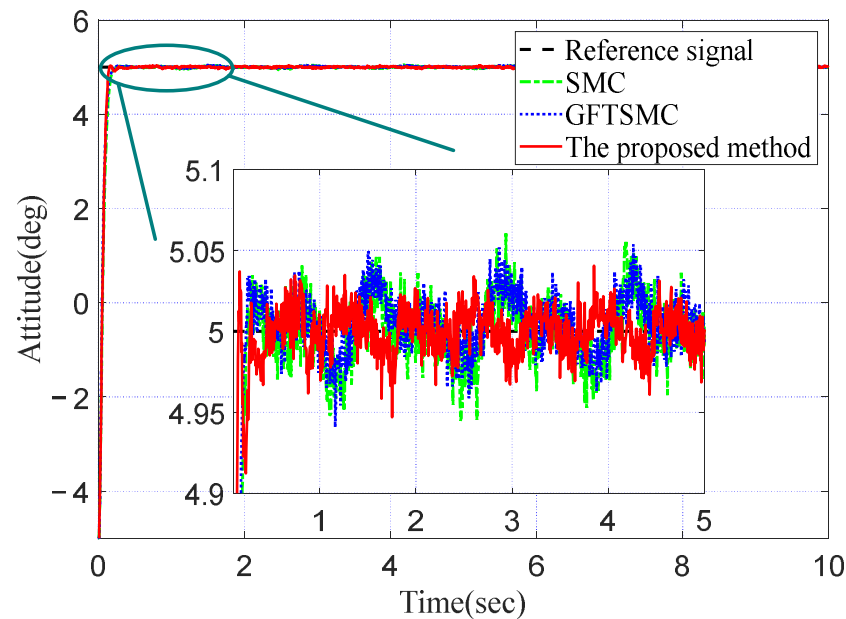


Figure 3. The control performances of different control methods.

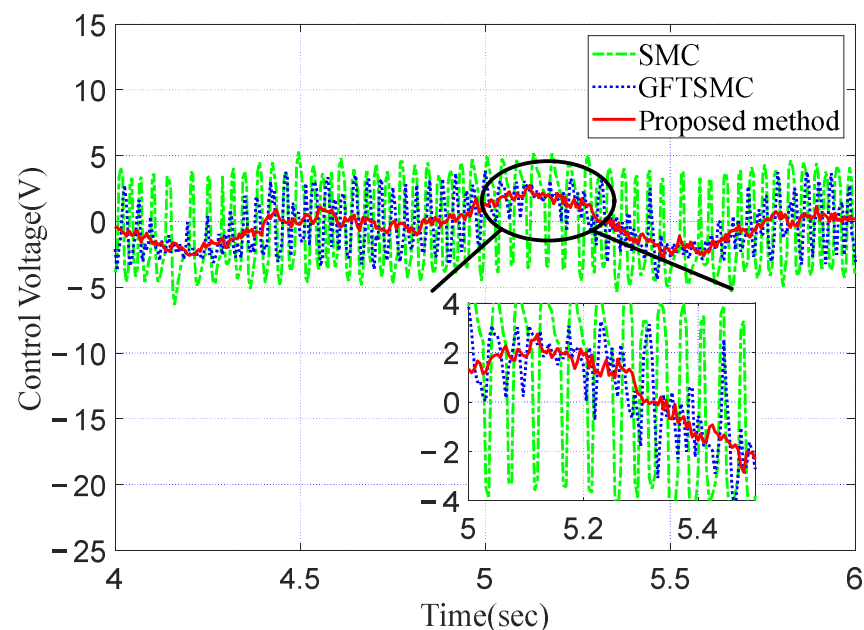


Figure 4. The control voltages of different control methods.

As can be seen from Figure 3, the three control schemes can achieve steady state within 0.3 s. Due to the influence of disturbances, the control curves have different degrees of oscillation. It is easy to see that the proposed control method has the best control

performance, and it can realize a fast response, such that the angle velocity can reach $66.7^\circ/\text{s}$. In order to depict the advantage of the proposed method, the indexes of the tracking error after reaching steady state have been calculated, including the root mean square error (RMSE), the integral of time-multiplied absolute value of error (ITAE), and the maximum deviation of error (MAXE).

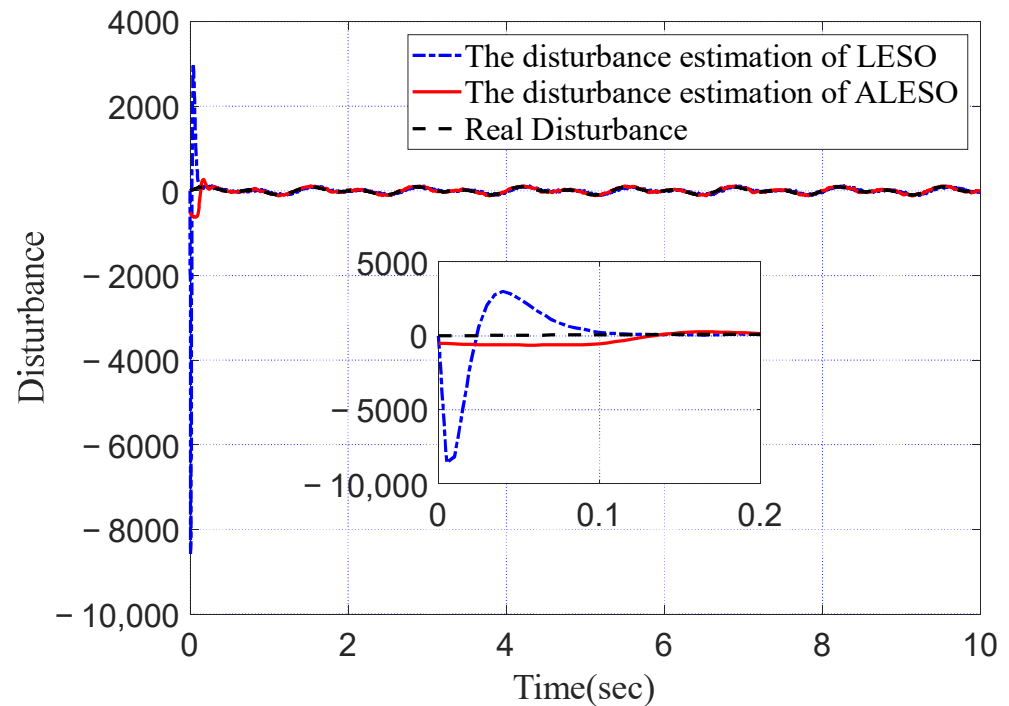


Figure 5. The disturbance estimations of LESO and ALESO.

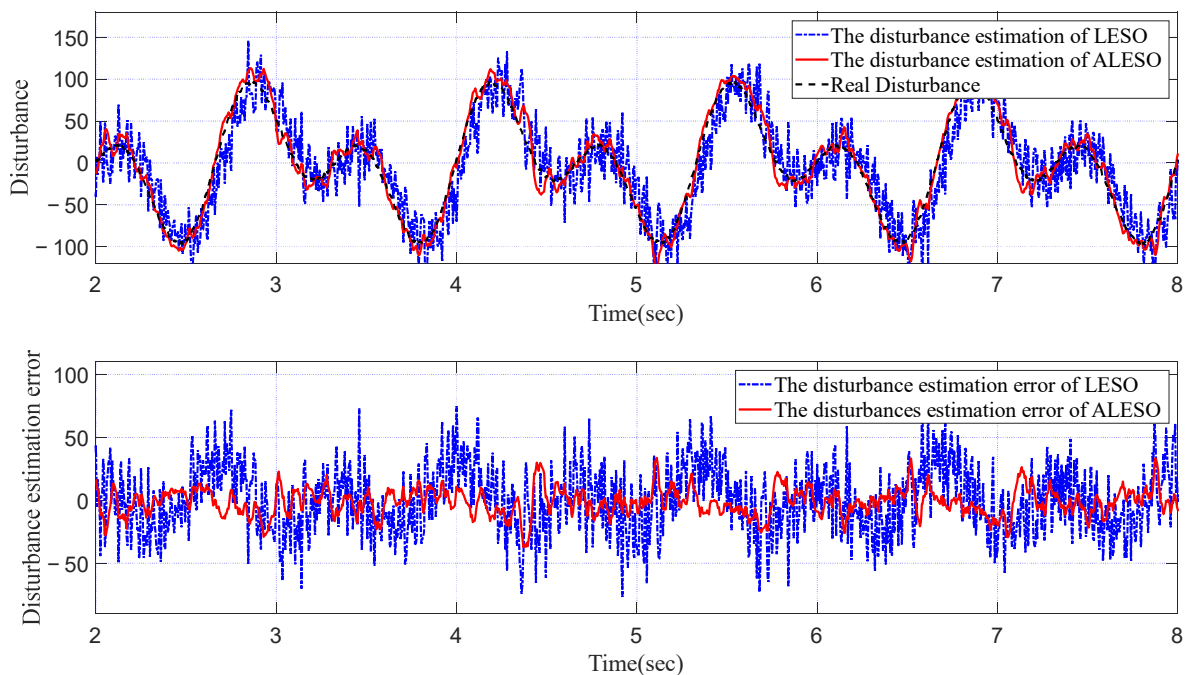


Figure 6. The disturbance estimations and errors of LESO and ALESO.

Table 2 shows RMSE, ITAE and MAXE values of the three controllers. Obviously, compared with the SMC and the GFTSMC, the RMSE value of the proposed method is improved by at least 24.2%, the ITAE value of the proposed method is improved by at

least 26.0%, and the MAXE value of the proposed method is improved by at least 10.6%. Table 2 signifies that, by the ALESO, the proposed control method has the best control performance, even if different kinds of disturbances exist.

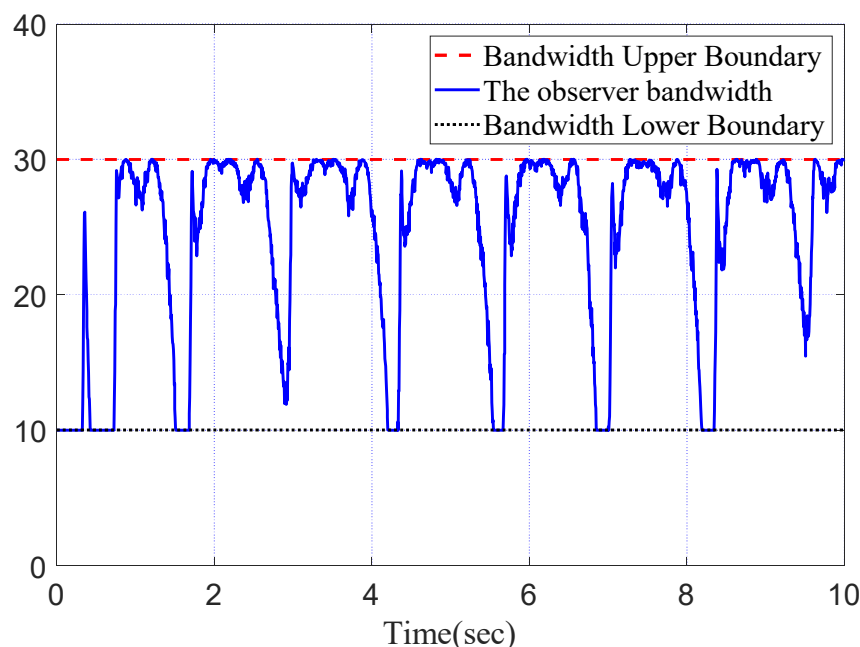


Figure 7. The observer bandwidth of ALESO.

Table 2. Comparisons of SMC, GFTSMC and the proposed method.

	RMSE	ITAE	MAXE
SMC	0.0203	0.1561	0.0605
GFTSMC	0.0186	0.1471	0.0595
The proposed method	0.0141	0.1089	0.0532
Improvements: SMC	30.5%	30.2%	12.1%
GFTSMC	24.2%	26.0%	10.6%

Figure 4 shows that although conventional GFTSMC does not contain the symbolic function $\text{sgn}(s)$, there is still a chattering problem in the control voltage of GFTSMC, which is unfavorable to the ISP system. Compared with the SMC and the GFTSMC, the proposed control can reduce the chattering problem, and the maximum control voltage generated by the proposed method is 2.898 V. That is nearly 45.7% of that of the SMC. It is very important for the ISP system because the ISP is supplied by the battery, and the small energy consumption means a long working time in the flight process.

Figures 5–7 show that the disturbance estimations of LESO and ALESO can track the disturbance within 0.15 s. Due to the continuous adaptive adjustment of the observation bandwidth and the disturbance estimation compensation, the estimation value of ALESO can deal with the peaking phenomenon without introducing excessive noise and can maintain a good estimation performance. Compared with the LESO, the ALESO has a better estimation accuracy. The maximum peak of estimation of ALESO is 621.3. That is only 7.24% of that of the former. In addition, the maximum disturbance estimation error of ALESO is around 20. That is only 33.4% of that of the former. At the beginning of the simulation, due to the large deviation between the initial states x_1, x_2 of the ISP system and the estimated states \hat{x}_1, \hat{x}_2 of the ALESO, from Figure 7 it can be seen that the bandwidth $\omega_A = \omega_{\min}$ was less than 0.5 s, and the ω_A gradually reached the maximum value ω_0 with the decrement of the estimation errors \tilde{x}_1, \tilde{x}_2 .

4.2. Experiments

Case 1: Vehicle Experiment

To further validate the performance of the proposed method, a vehicle experiment was carried out in the presence of linear motion, angular motion and vibration. The desired attitude angle $[\theta_{pd} \ \theta_{ad}]$ was set to $[0^\circ \ 0^\circ]$ to evaluate the disturbance rejection performance. As a comparison, the results obtained by the adaptive radial basis function neural network and back-stepping sliding mode control method (ANNSMC) of [25] is also displayed. In the vehicle experiment, the proposed method and ANNSMC were tested on a similar road and at a similar velocity.

Control performances, control voltages and disturbance estimations are shown in Figures 8–10. According to Figures 8–10, both the proposed method and the ANNSMC could estimate the disturbance, and the control voltages of them are both around ± 2 V, which facilitates the ISP system to run longer.

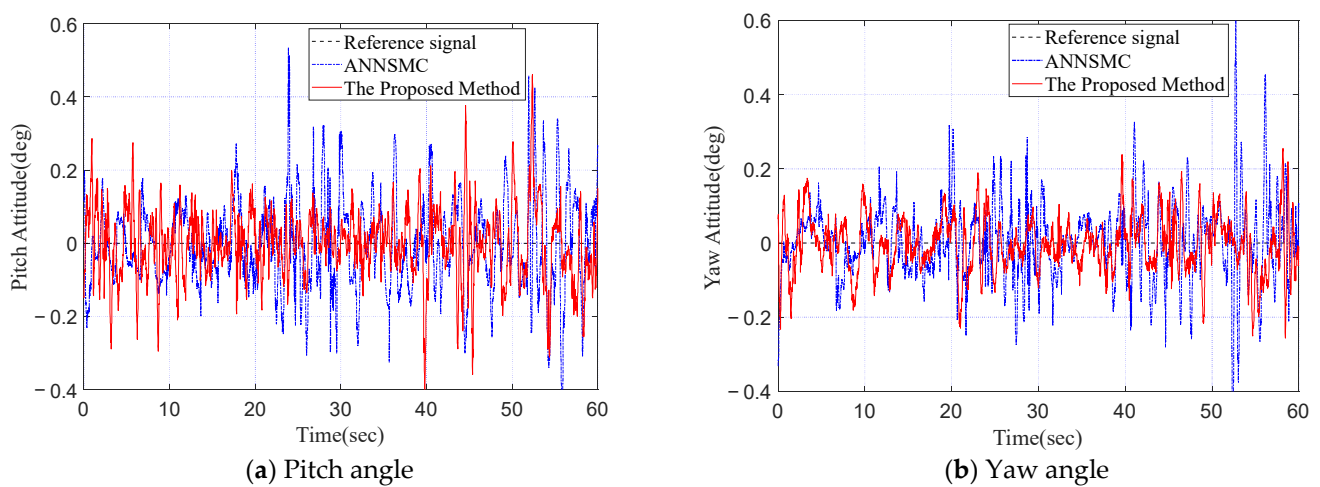


Figure 8. The control performances of the two controllers in Case 1.

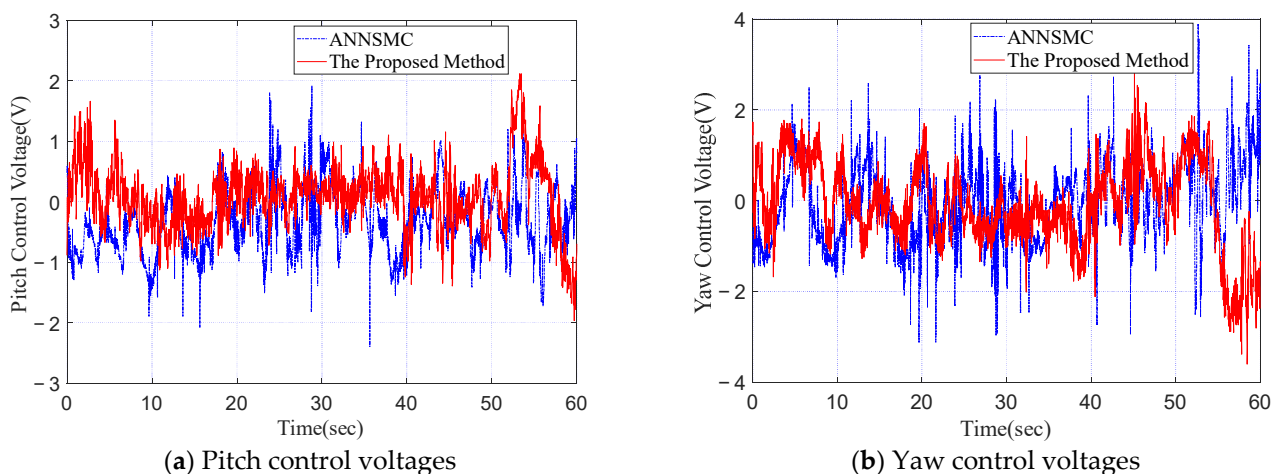


Figure 9. The control voltages of the two controllers in Case 1.

Table 3 shows RMSE, ITAE and MAXE values of the two controllers. Obviously, compared with the ANNSMC, RMSE value of the proposed method is improved at least 21.4%, ITAE value of the proposed method is improved at least 22.2%, and MAXE value of the proposed method is improved at least 13.8%. Table 3 shows that the proposed control method has the better control performance in Case 1.

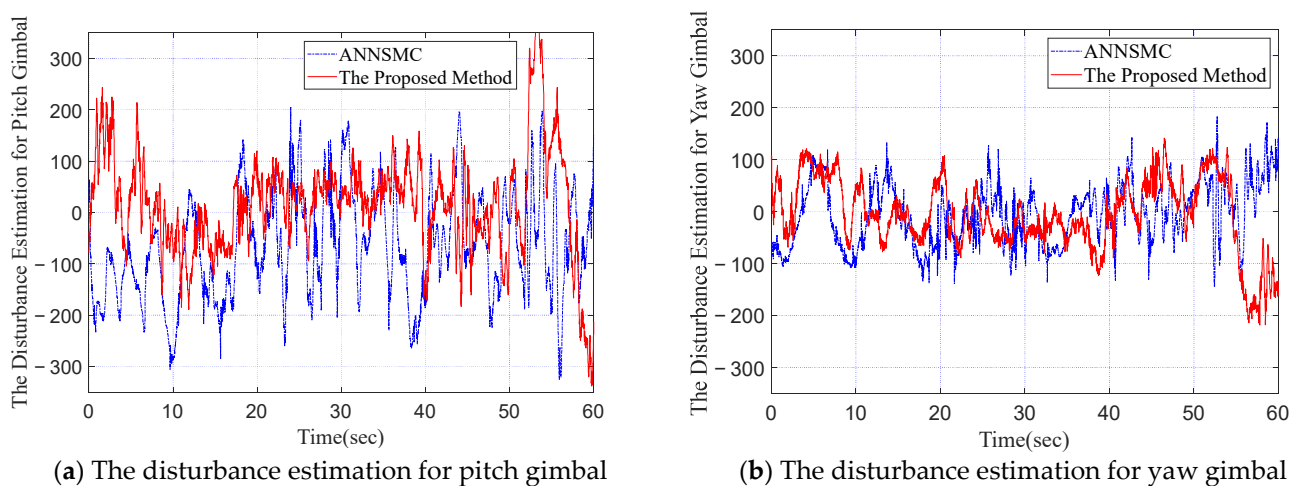


Figure 10. The disturbance estimations of the two controllers in Case 1.

Table 3. Comparisons of ANNSMC and the proposed method in Case 1.

	Pitch			Yaw		
	RMSE	ITAE	MAXE	RMSE	ITAE	MAXE
ANNSMC	0.1227	5.7368	0.5349	0.1022	4.4646	0.6045
The proposed method	0.0965	4.3419	0.4610	0.0753	3.4745	0.2560
Improvements	21.4%	24.3%	13.8%	26.3%	22.2%	57.6%

Case 2: Flight Experiment

To verify the effectiveness of the proposed method against complex disturbances, the intelligent inspection system finished a series of inspection tasks for 500 KV high voltage lines. The intelligent inspection system of the UH and ISP is shown in Figure 11. The ISP system is mounted at the bottom of the UH.



Figure 11. The intelligent inspection system.

The whole length of the high-voltage wire is 28 km. In addition, there are 12 electronic towers that should be inspected. Between two towers, the UH flew with the speed of 8 m/s. Based on the GPS information of the high voltage tower and UH, the ISP

automatically generates adjustment angle information. Then, the ISP was adjusted to track the high-voltage wire to get corresponding images. When the UH came to the nearby region of the tower, the speed of the UH was decreased to 2 m/s. At the same time, the ISP was adjusted to desired orientations for image acquisition. Each side of the high voltage tower was photographed and 3×5 photos were taken as a database for autonomous fault location. Since the long focus camera and short focus camera, infrared camera, ultraviolet camera, 3D laser scanner, and the POS were located in the settled positions of the pitch gimbal, the output of the POS was used as the criteria of the ISP system. To make a clear inspection for the high voltage tower, the common angular motion range of the pitch gimbal was from -70° to 10° because the common height of the 500 KV high voltage tower is 35 m. In addition, the common angular motion range of the pitch gimbal was 0° to 250° , due to consideration of energy consumption. For the ISP system, the pointing accuracy and quick response ability are the two main criteria in the task-finishing process.

The corresponding attitude angles of two gimbals generated by the proposed control method are shown in Figures 12 and 13. For the pitch angle, the MAXE is 0.38° and the dynamic response speed arrived at $97.89^\circ/\text{s}$. Moreover, the MAXE and RMSE of yaw angle are 0.12° and 0.018° , respectively. The ISP can realize a 40° adjustment of yaw angle in 0.48 s, such that the response speed can reach to $83.33^\circ/\text{s}$. When the outputs of the POS have come to the planned angles, the ISP can realize a high-performance steady control, such that the MAXE is less than 0.4° , and RMSE is less than 0.02° . Since the shutter time is $1/800$ s and there is nearly 4 s to executive tasks for the ISP in steady time, the ISP can realize a fast dynamic response and a high precise stabilization control for the high-voltage line inspection tasks.

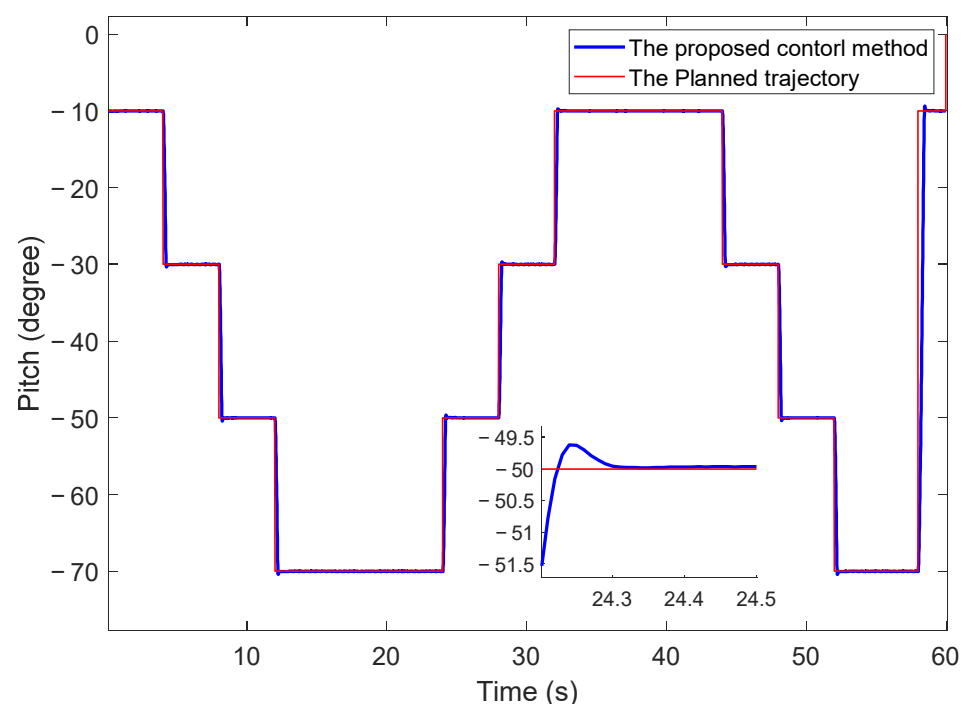


Figure 12. The flight trajectories of pitch gimbal in inspection test.

The intelligent inspection system finished 35 high-voltage line wire-inspection tasks. A total of 378 faults were located in the inspection process. The located faults of the spontaneous explosion of glass insulator string are shown in Figure 14.

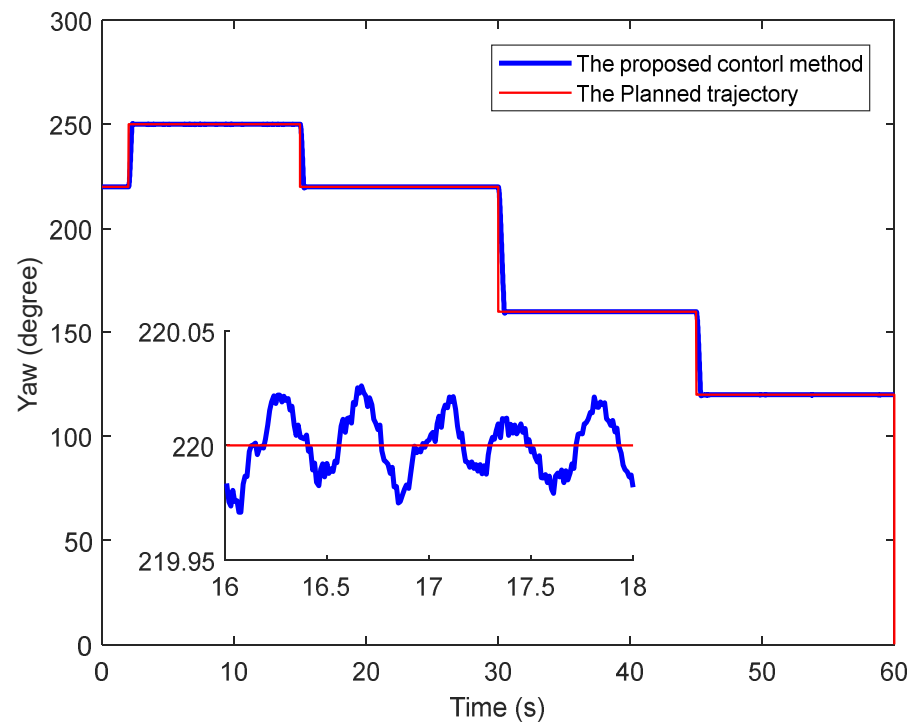


Figure 13. The flight trajectories of yaw gimbal in inspection test.



Figure 14. The located faults in the inspection.

5. Conclusions

To promote the control performance of the ISP system, a compound control method based on the ALESO and the GFTSMC was proposed. With the ALESO, the proposed control method can realize high-performance control for the ISP system in complex environments. Based on the proposed control method, the ISP system realized a fast dynamic response and high stabilization precision control performance in the high-voltage line fault location experiment. The ISP system can adjust the gimbals to isolate the non-ideal attitude perturbation of the imaging payloads. In the flight experiment, the root mean square error and the response speed of the ISP were 0.018° and $83.33^\circ/\text{s}$, respectively.

Author Contributions: Conceptualization, F.F.; methodology, X.L.; software, F.F.; validation, F.F. and X.L.; formal analysis, F.F. and X.L.; investigation, F.F. and X.L.; resources, F.F.; data curation, F.F.; writing—original draft preparation, F.F. and X.L.; writing—review and editing, F.F. and R.W.; visualization, F.F. and R.W.; supervision, F.F.; project administration, X.L.; funding acquisition, X.L. All authors have read and agreed to the published version of the manuscript.

Funding: This research was funded by the National Natural Science Foundation of China, grant number 61873016, 61633002, and 62173019.

Institutional Review Board Statement: Not applicable.

Informed Consent Statement: Not applicable.

Data Availability Statement: Not applicable.

Acknowledgments: Not applicable.

Conflicts of Interest: The authors declare no conflict of interest.

References

1. Masten, M.K. Inertially stabilized platforms for optical imaging systems. *IEEE Control Syst. Mag.* **2008**, *28*, 47–64.
2. Hilkert, J.M. Inertially stabilized platform technology Concepts and principles. *IEEE Control Syst. Mag.* **2008**, *28*, 26–46.
3. Zhou, X.; Zhang, H.; Yu, R. Decoupling control for two-axis inertially stabilized platform based on an inverse system and internal model control. *Mechatronics* **2014**, *24*, 1203–1213. [\[CrossRef\]](#)
4. Liu, S.; Che, H.; Sun, L. Research on stabilizing and tracking control system of tracking and sighting pod. *J. Control Theory Appl.* **2012**, *10*, 107–112. [\[CrossRef\]](#)
5. Fang, J.; Yin, R.; Lei, X. An adaptive decoupling control for three-axis gyro stabilized platform based on neural networks. *Mechatronics* **2015**, *27*, 38–46. [\[CrossRef\]](#)
6. Mu, Q.; Liu, G.; Lei, X. A RBFNN-based adaptive disturbance compensation approach applied to magnetic suspension inertially stabilized platform. *Math. Probl. Eng.* **2014**, *2014*, 464–483. [\[CrossRef\]](#)
7. Zhang, Y.; Yang, T.; Li, C.; Liu, S.; Du, C.; Li, M.; Sun, H. Fuzzy-PID control for the position loop of aerial inertially stabilized platform. *Aerosp. Sci. Technol.* **2014**, *36*, 21–26. [\[CrossRef\]](#)
8. Darestani, M.; Nikkhah, A.; Sedigh, A. H ∞ /Predictive output control of a three-axis gyrostabilized platform. *Proc. Inst. Mech. Eng. IMechE Conf.* **2013**, *228*, 679–689. [\[CrossRef\]](#)
9. Hou, S.; Chu, Y.; Fei, J. Intelligent global sliding mode control using recurrent feature selection neural network for active power filter. *IEEE Trans. Ind. Electron.* **2021**, *68*, 7320–7329. [\[CrossRef\]](#)
10. Jiang, B.; Karimi, H.R.; Yang, S.; Gao, C.; Kao, Y. Observer-based adaptive sliding mode control for nonlinear stochastic markov jump systems via T-S fuzzy modeling: Applications to robot arm model. *IEEE Trans. Ind. Electron.* **2021**, *68*, 466–477. [\[CrossRef\]](#)
11. Yu, X.; Man, Z. Fast terminal sliding-mode control design for nonlinear dynamical systems. *IEEE Trans. Circuits Syst.* **2002**, *49*, 261–264.
12. Yu, S.; Yu, X.; Man, Z. Robust global terminal sliding mode control of SISO nonlinear uncertain systems. In Proceedings of the 39th IEEE Conference on Decision and Control (Cat. No.00CH37187), Sydney, Australia, 12–15 December 2000; Volume 3, pp. 2198–2203.
13. Li, Y.; Qin, Y.; Wang, F.; Guo, F.; Yeow, J.T.W. Global fast terminal sliding mode control for a quadrotor UAV. In Proceedings of the 2020 15th IEEE Conference on Industrial Electronics and Applications (ICIEA), Kristiansand, Norway, 9–13 November 2020; pp. 1820–1825.
14. Liu, X.; Wang, Y.; Ji, Z. Global fast terminal sliding mode control system for permanent magnet synchronous motor drive under disturbances. In Proceedings of the 2018 37th Chinese Control Conference (CCC), Wuhan, China, 25–27 July 2018; pp. 3092–3095.
15. Lei, X.; Lu, P. The adaptive radial basis function neural network for small rotary-wing unmanned aircraft. *IEEE Trans. Ind. Electron.* **2014**, *61*, 4808–4815. [\[CrossRef\]](#)
16. Giap, N.H.; Shin, J.-H.; Kim, W.-H. Robust adaptive neural network control for XY table. *Intell. Control Autom.* **2013**, *4*, 8. [\[CrossRef\]](#)
17. Zou, Y.; Lei, X. A compound control method based on the adaptive neural network and sliding mode control for inertial stable platform. *Neurocomputing* **2015**, *155*, 286–294. [\[CrossRef\]](#)
18. Han, J. From PID to active disturbance rejection control. *IEEE Trans. Ind. Electron.* **2009**, *56*, 900–906. [\[CrossRef\]](#)
19. Liu, J.; Vazquez, S.; Wu, L.; Marquez, A.; Gao, H.; Franquelo, L.G. Extended state observer-based sliding-mode control for three-phase power converters. *IEEE Trans. Ind. Electron.* **2017**, *64*, 22–31. [\[CrossRef\]](#)
20. Yao, J.; Jiao, Z.; Ma, D. Adaptive robust control of DC motors with extended state observer. *IEEE Trans. Ind. Electron.* **2014**, *61*, 3630–3637. [\[CrossRef\]](#)
21. Sayem, A.H.M.; Cao, Z.; Man, Z. Model free ESO-based repetitive control for rejecting periodic and aperiodic disturbances. *IEEE Trans. Ind. Electron.* **2017**, *64*, 3433–3441. [\[CrossRef\]](#)
22. Ren, C.; Li, X.; Yang, X.; Ma, S. Extended state observer-based sliding mode control of an omnidirectional mobile robot with friction compensation. *IEEE Trans. Ind. Electron.* **2019**, *66*, 9480–9489. [\[CrossRef\]](#)
23. Pu, Z.; Yuan, R.; Yi, J.; Tan, X. A class of adaptive extended state observers for nonlinear disturbed systems. *IEEE Trans. Ind. Electron.* **2015**, *62*, 5858–5869. [\[CrossRef\]](#)

24. Li, P.; Zhu, G.; Zhang, M. Linear active disturbance rejection control for servo motor systems with input delay via internal model control rules. *IEEE Trans. Ind. Electron.* **2021**, *68*, 1077–1086. [[CrossRef](#)]
25. Dong, F.; Lei, X.; Chou, W. A dynamic model and control method for a two-axis inertially stabilized platform. *IEEE Trans. Ind. Electron.* **2017**, *64*, 432–439. [[CrossRef](#)]
26. Gao, Z. Scaling and bandwidth-parameterization based controller tuning. In Proceedings of the American Control Conference, Minneapolis, MN, USA, 4–6 June 2003; Volume 6, pp. 4989–4996.
27. Cheng, Y.; Ren, X.; Zheng, D.; Li, L. Non-linear bandwidth extended-state-observer based non-smooth funnel control for motor-drive servo systems. *IEEE Trans. Ind. Electron.* **2022**, *69*, 6215–6224. [[CrossRef](#)]
28. Yao, J.; Deng, W. Active disturbance rejection adaptive control of hydraulic servo systems. *IEEE Trans. Ind. Electron.* **2017**, *64*, 8023–8032. [[CrossRef](#)]